Influence of inertia relief analysis on the topological optimisation of unconstrained structures

Cristiam Javier Lasso Perdomo, Myriam Orquéra, Dominique Millet, Bertrand Gabriel

International Journal on Interactive Design and Manufacturing (IJIDeM)
https://doi.org/10.1007/s12008-024-02021-8

ORIGINAL ARTICLE

Influence of inertia relief analysis on the topological optimisation of unconstrained structures

Cristiam Javier Lasso Perdomo[1] · Myriam Orquera[1] · Dominique Millet[1] · Bertrand Gabriel[2]

Received: 14 March 2024 / Accepted: 15 July 2024

Abstract
The growth in build volumes of additive manufacturing (AM) printers has enabled the manufacture of larger and more complex products, such as drones, known as unconstrained structures. This necessitates advanced optimisation techniques to achieve optimal designs. Inertia relief (IR) is a solution for analysing these structures by leveraging their inertial properties while considering concentrated non-structural masses. Unfortunately, designers often overlook the benefits of IR due to a lack of understanding, a preference for static techniques involving boundary conditions (BCs), or the absence of a methodology for IR. Existing literature lacks sufficient comparison and documentation of the mechanical performance losses resulting from the application of BCs instead of IR. Therefore, this study provides a detailed comparison of BC and IR designs, highlighting the advantages in terms of compliance, stress fields, and eigenfrequency performance. Additionally, based on the findings, it proposes a comprehensive design and optimization methodology tailored for IR + TO, demonstrating its advantages through a case study. Applied to the redesign of a drone structure, results reveal that IR-optimized designs achieve a mass saving of 13%, with up to 53% lower compliance and 12%–32% lower stress values compared to BC-optimized designs. Those significant differences highlight the crucial role of IR in achieving optimal designs for unconstrained systems. Besides, these findings underscore the enhanced mechanical performance and potential for material savings in IR + TO, bridging the gap between theoretical understanding and practical application. This research provides valuable insights and practical guidelines for engineers and designers aiming to optimize complex structures for AM.

Keywords Inertia relief · Topology optimisation · Design methodology · Additive manufacturing · Drone · Airframe

1 Introduction

The rapid growth in the number of additive manufacturing (AM) applications has driven the development and redesign of new complex structures to meet today's challenges. Topology optimisation (TO) is a technique that allows a designer to take advantage of the freedom that AM offers, particularly for mass reduction [1], which was proposed by Bendsoe and Kikuchi [2]. Over the years, numerous methods have been developed to improve and extend its application, such as density-based methods, hard-kill methods, boundary variation methods, and a biologically inspired method, as reviewed by Deaton et al. [3]. Despite these developments, the density-based solid isotropic material with penalisation (SIMP) method remains the widest applied approach in commercial software and industry. One of its best-known applications is in the development of new mechanical structures, due to its great effectiveness in saving weight and improving multidisciplinary performance. Many authors have worked on deriving good practices for the use of TO; for example, Morretton et al. [4] showed that the final design is greatly affected by the settings adjustments made by the designer, whereas Tyflopoulos and Steinert [5] explored the ways in which the TO results are influenced depending on the boundary conditions (BCs), and Orquera et al. [6] examined the influence of the design space (DS) and non-design space (NDS). Its industrial applications were summarised in a review by Prathyusha et al. [7].

Over time, the applications of TO have been scaled up to include buildings, bridges, and transport systems such as aircraft [8] and vehicles [9]. These transport systems are commonly referred to as unconstrained structures (USs), as they

✉ Cristiam Javier Lasso Perdomo
classope134@etud.univ-tln.fr

1 COSMER Laboratory, Toulon University, Toulon, France

2 Expleo, Vitrolles, France

Published online: 29 August 2024

move through space as rigid bodies (RBs) without the need for physical supports to anchor them to a fixed frame. If traditional nodal displacement constraint methods were used to analyse these structures, the results would be artificially biased due to the presence of unrealistic reaction forces that would affect the stress field. To avoid this issue, designers are recommended to employ a technique known as inertia relief (IR), in which the inertial properties of the structure are used to counteract its motion and the system is then solved.

Barnet et al. [10] introduced this approach, and researchers have since formulated and published other types of IR procedures and applications. Essentially, applied loads produce RB translational and rotational accelerations, and when combined with the mass and inertia of the structure, induce RB inertia forces distributed over it. By subtracting the inertial forces from the external forces, the elastic forces produce a load-balanced static formulation, allowing the designer to determine the displacements and stresses, as described by Lee and Guo [11] and Wijker [12].

Applications of this method can be found in numerous published works: for example, Nelson and Wolf used this approach to replace a transient dynamic analysis to estimate impact loads on a structure [13]; De et al. [14] applied it to the design of a lightweight chassis for a hybrid truck; and Liao [15] studied the implementation of basic structures and the influence of conventional and automatic setups, constraints and mass distribution In the field of TO, Pagaldipti and Shyy [16] explored the impact of IR and local mass on TO, and Wagner and Helfrich [17] extended this research by applying it to the optimisation of a control arm. Song et al. [18] proposed a TO formulation based on regional strain energy for the optimisation of protective structures, and Thore [19] provided a detailed explanation of the TO and IR theory and compared 3 methods of problem-solving.

Although the use of IR with TO has been considered in previous works, these studies have mainly focused on mathematical development or specific applications like single parts. Then, looking to the TO for USs like drones, studies such as those by [20–22] commonly apply traditional BCs by fixing either the centre of the main body or the arms. Relatedly, others like [23] split the model into components and optimised them independently. Similar cases were found during the literature review and are summarised in Table 6 in the Appendix of this paper. Unfortunately, the preference for static techniques involving BCs, coupled with a lack of understanding or absence of an IR methodology, often leads designers to overlook the benefits of IR. This can result in suboptimal designs due to the artificial constraints imposed by the BCs. Consequently, a significant question arises: how much does the use of BC-modelling versus IR-modelling impact the optimal design of a structure?.

1.1 Article scope

Up to now, there has been a lack of awareness and clarity in the literature regarding IR, particularly when comparing the mechanical performance drawbacks of IR-optimised designs to those incorporating BCs. Furthermore, the state of the art highlights the absence of a method for optimizing USs using IR. Hence, this paper aims to explore the drawbacks that arise when BCs are applied to an US. It provides a detailed comparison, highlighting the advantages of applying IR in terms of compliance, stress field, and eigenfrequency performance. By proposing a design and optimisation methodology adapted to IR + TO, this contribution bridges the gap between the current theoretical understanding of IR and its practical application in structural optimisation.

To achieve this objective, the article is structured as follows: Sect. 2 introduces the mathematical background of IR and highlights the parameters that affect the elastic forces. TO is then presented, and how it can be combined with IR in the optimisation formulation is subsequently explained. Afterwards, the optimisation of 2 USs will be conducted, with one approach applying BCs and the other IR. For the sake of clarity, the former will henceforth be referred to as BC-design and the latter IR-design. The results comparison highlights the drawbacks of the BC-design. Thanks to the findings, a methodology for TO + IR is proposed in the Sect. 5. A case study is presented to demonstrate the application of our methodology to the redesign and optimisation of a drone airframe. In this way, the discussion compares traditional modelling based on BCs with IR and observes the percentage gains obtained. To conclude, the article will deal with the conclusions and perspectives.

2 Mathematical background

2.1 Inertia relief

This technique approximates a dynamic problem as a static one, based on the following assumptions: (i) the structure moves through the space as if it were infinitely stiff, and (ii) the loads are in a steady state meaning that the structure is under constant loads and accelerations. The fundamental equation can then be derived from an approximation of the dynamic equilibrium equations of motion:

$$[M]\{\ddot{u_t}\} + [K]\{u_t\} = \{F_{ext}\} \tag{1}$$

where $[M]$ is the mass matrix,$[K]$ the stiffness matrix, and $\{F_{ext}\}$ the external force vector. The first assumption is then expressed through the total displacement vector, denoted as $\{u_t\}$, which comprises both the RB $\{u_r\}$ and the elastic $\{u_e\}$

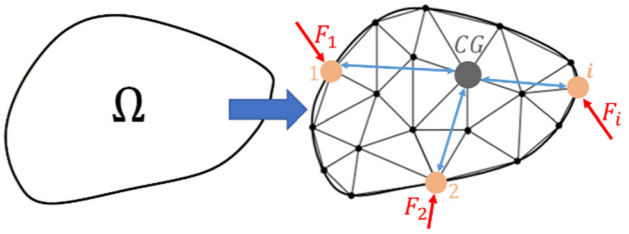

Fig. 1 Reference point for the equilibrium of a rigid body

vectors. Where the last one results from the elastic deformation of the body under inertial forces, as follows:

$$\{u_t\} = \{u_r\} + \{u_e\} \tag{2}$$

Assumption (i) leads to $[K]\{u_r\} = 0$, and assumption (ii) to the simplification $[M]\{\ddot{u_e}\} = 0$. Consequently, Eq. (2) can be reformulated as:

$$[M]\{\ddot{u_r}\} + [K]\{u_e\} = \{F_{ext}\} \tag{3}$$

To solve this problem, the finite element method is commonly employed. However, due to the absence of BCs, the system becomes singular. In such cases, 3 possible methods can be applied [19]. The first, known as the geometrical centre (CG) method, is explained below. After discretising the body, IR forces are calculated based on the RB modes and $[M]$. To achieve this, a reference point, typically the CG (Fig. 1), is chosen to apply the transformations required for the equilibrium and to handle the singularity of the stiffness matrix by imposing a displacement.

For equilibrium of the forces and moments at CG, the RB transformation matrix of each node i_{th} $\left[\Phi_{i,0}\right]$ relates the motions of the RB from the CG $\left\{u_{r,\,p_0}\right\}$ to the motions of each node i_{th} $\left\{u_{r,i}\right\}$. We can then define:

$$\left\{u_{r,i}\right\}=\left[\Phi_{i,0}\right]\left\{u_{r,\,p_0}\right\} \tag{4}$$

where x_i, y_i, z_i are the coordinates of each node i_{th}, and x_0, y_0, z_0 denote the coordinates of CG.

$$\left[\Phi_{i,0}\right] = \begin{bmatrix} 1\,0\,0 & 0 & (z_i - z_0) & -(y_i - y_0) \\ 0\,1\,0 & -(z_i - z_0) & 0 & (x_i - x_0) \\ 0\,0\,1 & (y_i - y_0) & -(x_i - x_0) & 0 \\ 0\,0\,0 & 1 & 0 & 0 \\ 0\,0\,0 & 0 & 1 & 0 \\ 0\,0\,0 & 0 & 0 & 1 \end{bmatrix}$$

From this matrix, in the case of rotational acceleration, the further the i_{th} node is from CG, the higher its acceleration will be. To calculate the stresses in the structure, the second term in Eq. (3) must be solved, which can be represented as $[K]\{u_e\} = \{F_{el}\}$. Here, the external forces $\{F_{ext}\}$

Fig. 2 Compression static analysis with IR: **a** model; **b** von Mises stress field

are assumed to be in equilibrium with the RB inertia forces $\{F_r\}$ and the internal elastic forces $\{F_{el}\}$, where the latter are derived from subtraction as follows:

$$\{F_{el}\} = \{F_{ext}\} - \{F_r\} \tag{5}$$

The vector $\{F_r\}$ is responsible for the virtual movement of the body and is defined as being in equilibrium with the inertial loads $[M]\{\ddot{u}_r\}$:

$$\{F_r\} = [M]\{\ddot{u}_r\} \tag{6}$$

The acceleration vector for the RB, $\{\ddot{u}_r\}$, can be expressed as a linear combination of the global RB body transformation matrix $[\Phi_r]$; this contains the transformation matrix of each node i_{th} $\left[\Phi_{i,0}\right]$ and the vector $\left\{\ddot{u}_{r,\,\mathrm{p}_0}\right\}$, which represents the acceleration of each of the rigid body modes at the reference point, as shown in Eq. (7). The same principle can be applied to the RB inertia forces $\{F_r\}$, as given in Eq. (8):

$$\{\ddot{u}_r\} = [\Phi_r]\left\{\ddot{u}_{r,\,\mathrm{p}_0}\right\} \tag{7}$$

$$\{F_r\} = [\Phi_r]^T\{F_{ext}\} \tag{8}$$

By substituting Eqs. (6) and (7) into Eq. (8), we can derive Eq. (9):

$$\left\{\ddot{u}_{r,\,p_0}\right\} = \left([\Phi_r]^T[M][\Phi_r]\right)^{-1}[\Phi_r]^T\{F_{ext}\} \tag{9}$$

Finally, by substituting Eqs. (9), (7) and (6) into Eq. (5), the internal elastic forces $\{F_{el}\}$ are obtained as shown in Eq. (10). This allows the stresses and displacements of the structure to be found.

$$\{F_{el}\} = \{F_{ext}\} - [M][\Phi_r]\left([\Phi_r]^T[M][\Phi_r]\right)^{-1}[\Phi_r]^T\{F_{ext}\} \tag{10}$$

Equation (10) defines how the mass and the transformation matrix influence the result of the elastic force vector. As highlighted by Wijker [12], in a structure consisting of homogeneous masses, the one to which the force is applied will have the highest elastic force value as a result. This is illustrated in Fig. 2, where an unconstrained beam is subjected to an external load. In response, IR induces a body

load to counterbalance the applied load, resulting in a stress field extending from the load point application to the end of the beam.

2.2 Topology optimisation

This mathematical method allows to determine the optimal material distribution within a given DS, to achieve an objective while meeting a set of constraints. The most common formulation ($\mathbb{P}_1$) involves minimising the elastic deformation energy or the so-called compliance (C) under a volume constraint [4]. The TO problem can therefore be stated as follows:

$$find \eta = (\eta_1, \ldots, \eta_i),\ 0 < (\eta_i)_{min} < \eta_i \leq 1,\ i = 1, \ldots N$$

$$(\mathbb{P}_1) = \begin{cases} \min C(\eta) = \frac{1}{2}\{F_{ext}\}^t\{u\} \\ s.t. \begin{cases} [K](\eta)\{u\} = \{F_{ext}\} \\ V(\eta) = \sum_{i=1}^{N} v_i \eta_i \leq V_U \end{cases} \end{cases} \tag{11}$$

where η is the artificial density vector containing all the design variables, N the total number of elements, C the compliance, $\{F_{ext}\}$ the external force vector, $[K]$ the stiffness matrix, $\{u\}$ the displacement vector, v_i is the volume of each finite element, and V_U the volume constraint value.

The pseudo-density from the SIMP model is employed here, which gives the following power-law relation for the stiffness and the value of the intermediate densities:

$$E_i = \eta_i^p E_0,\ p > 1 \tag{12}$$

where p represents a penalty coefficient for the stiffness of the material, and E_0 is the Young's modulus. Finally, to improve the discretisation and to control the size of the topology 'frames', multiple parameters can be applied: these include a minimum (MinDim) and maximum (MaxDim) size control method to filter out very thin or large frames [3, 24]; a minimum that adds a penalty based on the distance between the frames (MinGap) [4]; symmetries along one, 2 or 3 planes; pattern repetitions; or manufacturing constraints [25].

2.3 Topology optimisation with IR

The optimisation problem with IR requires a change in ($\mathbb{P}_1$), as indicated in Eq. 13. In this case, elements of $[M]$ are calculated from ($m_i = v_i \rho_i$), where $\rho_i = \eta_i \rho_0$, and ρ_0 is the density of the material.

$$s.t. \begin{cases} [M]\{\ddot{u_r}\} + [K]\{u_e\} = \{F_{ext}\} \\ V(\eta) = \sum_{i=1}^{N} v_i \eta_i \leq V_U \end{cases} \tag{13}$$

An example of the presence or the absence of BCs can be seen in the work of Quinn [26], as illustrated in Fig. 3. In the conventional BC-design (Fig. 3a), TO generates a design by following the stress flow from the point of application of the load to the fixed supports. However, in the IR-design (Fig. 3b), the mass is concentrated close to the point of application since there is no stress path as in the previous approach. Consequently, applying BCs can significantly impact the resulting design, due to a wrong description of the physical system.

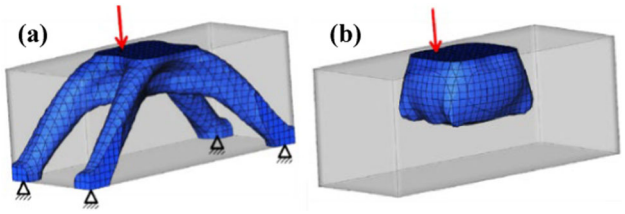

Fig. 3 Comparison of TO results for a brick: **a** conventional BC-design; **b** IR-design for an unconstrained structure. Adapted from Quinn [26]

3 Research method

To emphasise both the importance of applying IR to the optimisation of USs (as opposed to a BC approach), and to outline the considerations required for designing under IR, 2 distinct approaches are proposed:

- In the first study, we optimise common structures using BC and IR designs. The results are then compared and the differences between them are highlighted. The outcomes of the study allow us to propose a methodology for IR + TO.
- The second study demonstrates the application of the proposed method. The research strategy is illustrated in Fig. 9. The proposed methodology is implemented to guide new designers. The results of this second study are compared to those of a BC-design approach, to accentuate the advantages of the proposed method.

4 Influence of the design approach: topology optimisation with BCs vs. IR

As aforementioned, the topology obtained through IR differs from one obtained using BCs. It can therefore be inferred that when optimising an IR problem with BCs, the resulting topology may not be the most optimal. To illustrate this hypothesis, 2 structures that normally operate under dynamic conditions are optimised through BC-design and IR-design. They are then submitted to an IR analysis, and the results are finally analysed and discussed.

The TO models described below were implemented using Altair software with (i) HyperWorks used to realise example (a) and the study case; (ii) Inspire for example (b). The simulations were conducted on an Intel Core i7-11850H with 32 GB of RAM. The units employed were mm, N, g, and MPa. Each model was identical in terms of dimensions, loads, BCs, and optimisation formulations as in the original studies. In certain models, multipoint constraints (RBE2 or RBE3) were applied to model the connections, loads, and BCs. The first element (RBE2) introduces infinite stiffness to the nodes that are constrained, while the second (RBE3) provides a distributed connection that does not influence the local (or global) stiffness of the model. This is ideal for load/mass distribution [27].

Following optimisation, models were generated using automatic interpretation (OSSmooth) for reanalysis in HyperWorks. This was achieved by specifying a density threshold, and the option 'keep smooth narrow layer around non-design' option. Subsequently, all elements were then 'split' and transformed to 'second order' to further refine the model.

4.1 Control arm

The first model was one proposed by Altair [28]. The BCs are represented as triangles in Fig. 4a and b, and the associated degrees of freedom (DOF) are given as numbers. The study involved a single load case with 2 forces, as shown in Fig. 4c: (i) in the z-direction, with a magnitude of $3e5$ N; and (ii) in the x-direction, with a value of $-1e5$ N. The material was steel with a Young's modulus of $210e3MPa$, a Poisson's coefficient of 0.3, a density of $7.86e-3g/mm^3$, and a yield strength of 520 MPa. The FEM model was composed of CHEXA8 elements with a size of 6 mm. The optimisation formulation applied was the $\mathbb{P}_1$ within a volume constraint of 20%. A symmetry plane (x) and a MinDim of 40 were imposed as additional parameters.

Models were generated based on the thresholds in Table 1 to ensure the same volume. Results show that the BC-design includes the anchor zone for the shock absorber, while the IR-design does not, as shown in Fig. 6a and b. The reason is that in IR, displacements are relative, and do not influence the stress field. Hence, the use of special 'supports' for IR analysis, to replicate the deformation behaviour according to the arm movement, does not guarantee a stress flow through that area, resulting in a low-density region from the obtained topology, as mentioned in [19]. Therefore, to ensure the future connection of the shock absorber, 2 potential adjustments can be considered: The shock absorber mass can be included, or a new NDS can be specified, as shown in the zone with a star shape, enclosed by a circle in Fig. 5.

The results in Fig. 6a–c and Table 1 show that the compliance and stress values for the IR-design are lower by 34.7% and 12–32%, respectively, in comparison to the BC-design. The IR-design with the NDS modification has a similar performance. This demonstrates that IR models outperform those based on BCs. The cause may be intimately related to

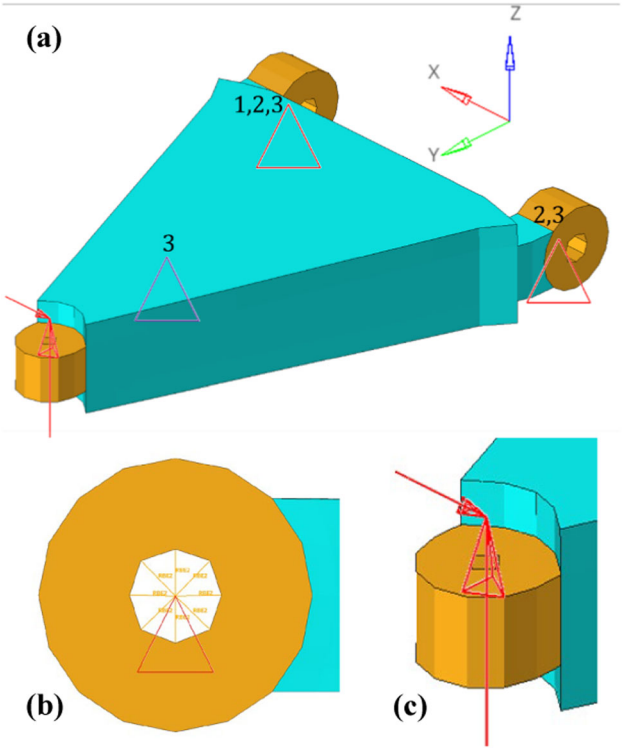

Fig. 4 Benchmark problem for TO, involving a control arm from Altair [28]: **a** locations of BCs; **b** detail showing the application of BCs with RBE2; **c** load point of application

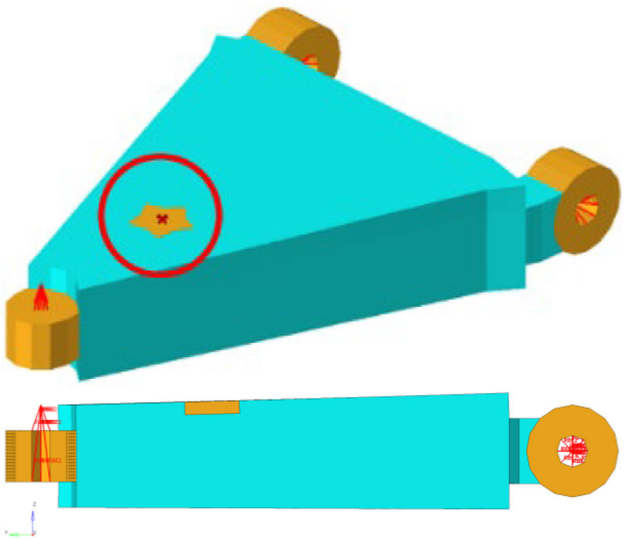

Fig. 5 New non-design space for the control arm (orange area shown in the red circle)

Table 1 Summary of results for the control arm

Values/models	BC-design	BC-designIR analysis	IR-design	IR new NDS design
Threshold	0.25	0.275		
Volume DS (e6 mm^3)	1.64	1.60		
V. DS + NDS (e6 mm^3)	2.01			
Compliance (e5 Nmm)	3.60	2.19	1.43	1.47
Ixx (mm^4)	275.1	277.8	278.9	
Iyy (mm^4)	115.4	158.6	151.9	
Izz (mm^4)	369.3	413.0	406.0	

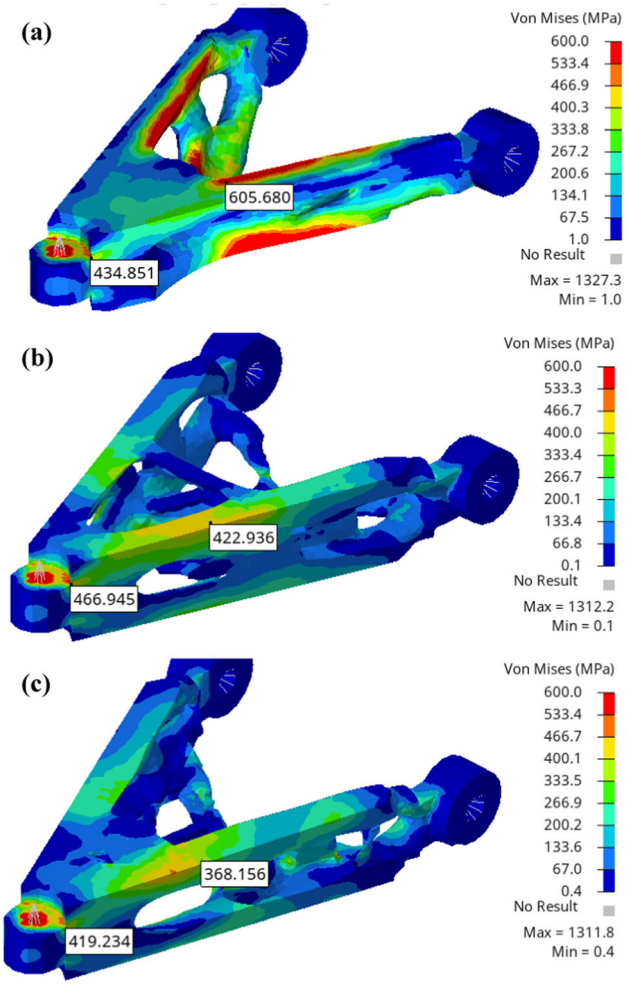

Fig. 6 Stress analysis of the control arm: **a** BC-design; **b** IR-design; **c** IR-design with the DS modified

the higher inertia values for I_{yy}(37%) and I_{zz} (12%) in the IR-designs, as shown in Table 1. These inertias counteract the stresses generated by the moments and the torque created by the forces. Finally, the modification proposed for IR-design allows the shock absorber anchor zone to be retained (Fig. 6c).

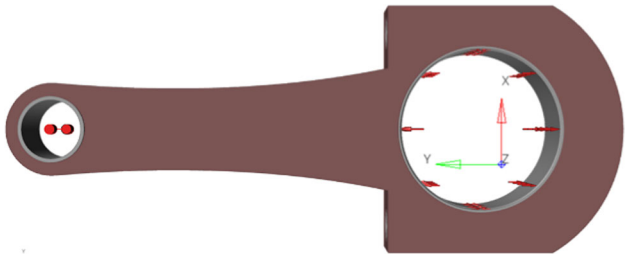

Fig. 7 Finite element model of a connecting rod considered by Orquera et al. [6]

4.2 Connecting rod

Another model that highlights the advantages of IR + TO is the connecting rod analysed by Orquera et al. [6]. In this study, optimisation was conducted using classical BC modelling. The bearing of the connecting rod at the small end is clamped, and the large rotating bearing is loaded. Two different load cases are considered: (i) a tensile force of $11449N$; (ii) a compression force of $27721N$. These load cases are depicted in Fig. 7. We note that in the IR model, only the loads are applied. The material was TiAl6V with a Young's modulus of $131.5e3MPa$, a Poisson's coefficient of 0.31, a density of $4.5e{-}3g/mm^3$, and a yield strength of $1110MPa$. The FEM model was constructed with a mesh size of 2 mm.

In this example, the objective is to maximise both the stiffness and the eigenfrequency. To achieve this, a new optimisation formulation is employed, designated as ($\mathbb{P}_2$), which introduces the combined compliance index response (S). This response allows to minimise the strain energy (C_i) and maximise the inverse of the eigenvalues (λ_j), as shown in Eq. (14). Given the substantial difference in the orders of magnitude between (C_i) and (λ_j), a normalization factor is used ($NORM = C_{max}\lambda_{min}$), in which the largest value of compliance and the lowest eigenvalue obtained in the first iteration are multiplied. This normalises the eigenvalue and gives a value between zero and one. This is then multiplied by the largest value of the compliance, to achieve a total value on the same order of magnitude as the sum of the compliances. For further details, please refer to [29]. By default, Inspire

Table 2 Summary of results for the connecting rod

Values/models	BC-design	BC-design IR analysis	IR-design
Mass DS (g)	212	219	
Compliance $e7(Nmm)$	2.37	0.62	0.39
First eigenfrequency (Hz)	3222	3954	3615

maximises the first 6 eigenfrequencies.

$$S = \sum_i W_i C_i + NORM\left(\frac{\sum_j \left(\frac{W_j}{\lambda_j}\right)}{\sum_j W_j}\right) \tag{14}$$

The constraints were a maximum volume of 35% and 2 planes of symmetry in the directions (x, z). In their original work, Orquera et al. [6] perform multiple optimisation loops to redesign the NDSs to the topologies found. However, in this work, only the first optimisation is required to compare the BC and IR outcomes.

For reconstruction, we used the 'topology slider' offered by Inspire to adjust the amount of material finely. This slider was positioned in the middle for each model to obtain the same mass. The results are summarized in Table 2.

We then evaluated the compliance obtained from a static analysis under IR. The IR-design values were found to be 37% lower in comparison to the BC-design. Following the research by Orquera et al. [6], the first eigenfrequencies of each model were then compared, and it was observed that the IR-design performed 8.5% better than the BC-design. Finally, for the stress values, the 'results envelope' option was applied, which provides the maximum value for each type of result across all load cases. Compared to BC-design, the values yielded by IR-design were lower by 72% on average (Fig. 8a, b). At the lower connection (Fig. 8c, d) of the bearing at the large end, we see that the BC-design has higher stress concentrations.

Finally, a noteworthy change in the new topology was the displacement in the location of the CG, which moved from 41.5 mm (BC) to 26.3 mm (IR), toward the flange of the crankshaft. This shift could potentially reduce the longitudinal vibrations.

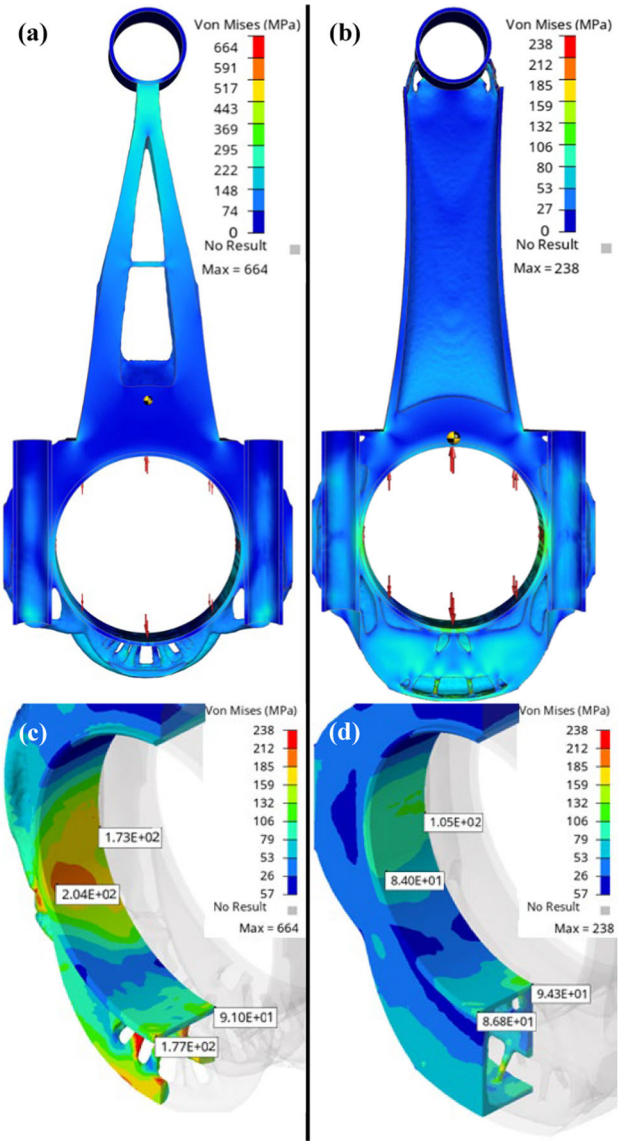

Fig. 8 von Mises stress fields for the connecting rod; **a**, **c** BC-design [6]; **b**, **d** IR-design

5 Proposed methodology

The models analysed above showed that optimisation without IR affects the results and decreases the performance. However, the simplicity of these models means that they do not consider other phenomena, such as the influence of local masses or how forces are transmitted to the structure. It can therefore be inferred that when analysing complex structures such as drones or aircraft, optimising them with BCs will have an even greater impact. Consequently, we propose a design methodology for the optimisation of USs, based on previous DfAM works [30–32]. It consists of ten steps, starting with the requirements and ending with splitting for assembly or fabrication, as shown in Fig. 9.

1. *List of requirements* This includes the performance, behaviour, functions, or systems that the structure must possess to satisfy the user's needs. For example, the structure of a helicopter will involve energy absorption,

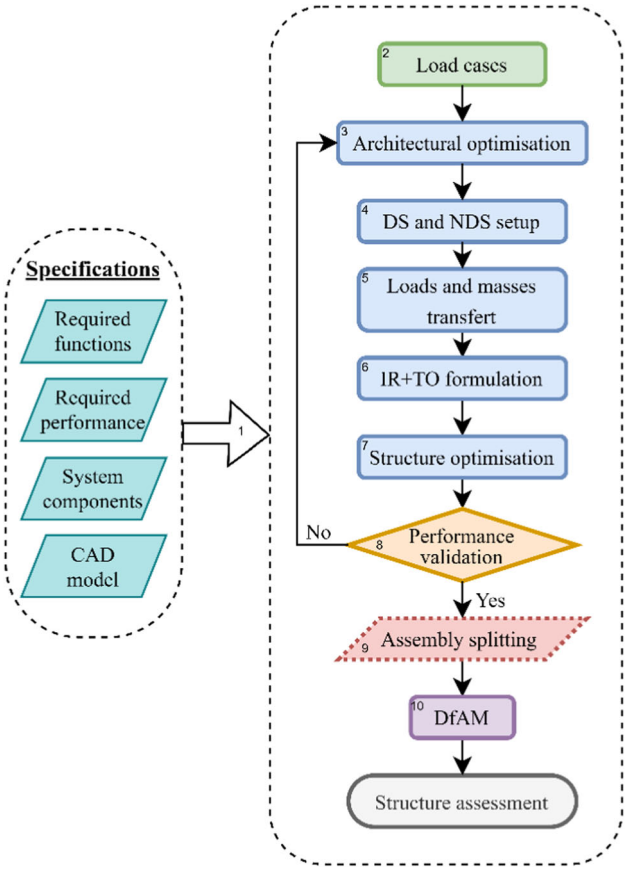

Fig. 9 Proposed methodology for inertia relief optimisation of additive manufacturing

the integration of pipes, a safety factor, and structural stability [30].

2. *Load cases* All the loading conditions to which the structure will be subjected, such as nominal, dynamic, or impact conditions, must be identified and established.
3. *Architectural optimisation* As reported by Wagner [17], and highlighted by Liao [15] 'the variation of mass distribution leads to the change of the distribution of inertia forces and moments, which results in different deformation and stresses'. Consequently, to achieve a desired behaviour, it is crucial to know the architecture and placement of components within the DS. This can involve establishing criteria such as: (i) achieving a balance around a reference point; for example, in a helicopter, considerations may include the seating arrangement and placement of luggage [33]; (ii) the limitations imposed by dimensions, as demonstrated by Ramsaier et al. [34], where modifying the position of the battery, motor, or propellers leads to changes in the topology of the structure as it adapts to new constraints; (iii) the positioning based on their functionality; for instance, in the design of a helicopter, this would include the placement of rotors, landing gear and fuel storage [35].
4. *DS and NDS setup* The DS has a strong influence on the final topology and mechanical behaviour [4–6]. A large DS allows exploring different stress fields, and, often, to obtain a stiffer design. The previous step will also impose NDSs such as: (i) volume occupied by components, (ii) contact or coupling surfaces, and (iii) surfaces or volumes to fulfil functions (movement, fluid conduction, etc.).
5. *Connection of loads and masses* Once the components and loads have been identified, another fundamental aspect is how loads are transmitted to the structure, as in IR, the stress path is very sensitive. For this reason, the anchorage points of the standard components of the structure must be considered. For the other components, we can assume a DS, NDS or functional surface on which they will be placed.
6. *TO formulation* Based on the specified requirements, the formulation will be chosen. In this work, 3 formulations were presented and assessed.
7. *Structure optimisation* The model is created by defining the BCs, load cases, DS, NDS, and formulation. The TO process is then carried out.
8. *Performance validation* When optimisation is complete, the results must be interpreted. The obtained structure is then analysed to validate the design, based on the parameters and design constraints established in the first step.
9. *Assembly splitting (if desired)* There are several reasons to split a structure into components, as described by Reichwein et al. [36]. This step may be performed based on the designer's experience, zones with fewer stresses or a higher density concentration.
10. *Design for manufacturing* The last step is related to the constraints arising from the manufacturing process, due to the technology or the material chosen. The methodology proposed in [36] can be followed.

6 Case study: structure of a drone

A literature survey was conducted to select a predefined model. The keywords employed for the research were: 'drone' OR 'UAV' OR 'quadcopter'; 'structure' OR 'airframe'; 'design' OR 'optimisation' OR 'sizing'; 'inertia relief'; and 'optimisation', 'topology optimisation' OR 'generative design'. The articles found are categorised as follows: 2 reviews provided classifications, applications, and design challenges [37, 38]; 13 focused on flight control equations, the estimation of flight times, and the selection of components; 24 focused on the design, analysis, or optimisation of

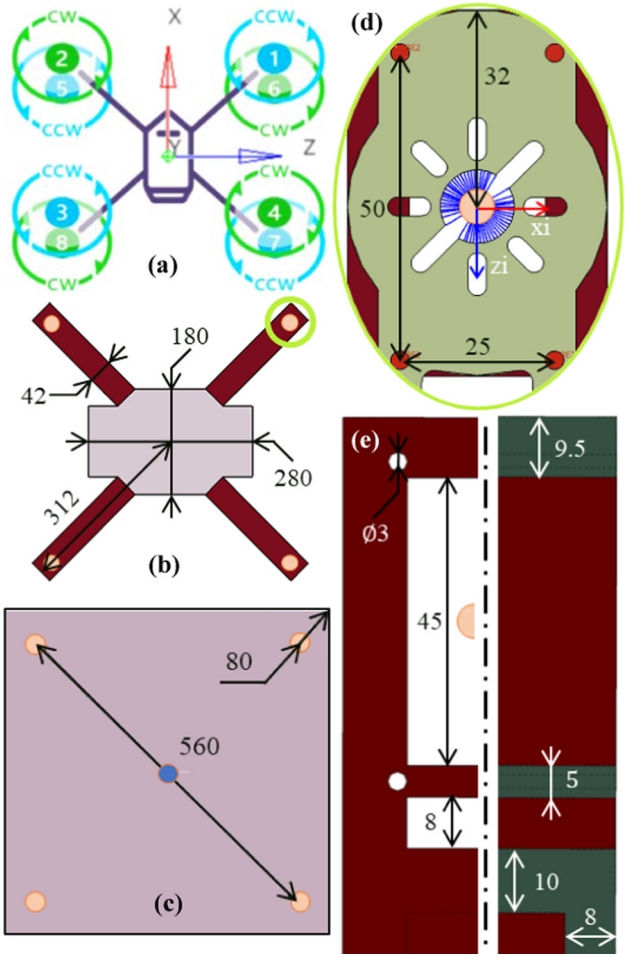

Fig. 10 Model used for the study: **a** architecture of the drone; **b** original DS set-up; **c** enlarged DS set-up; **d** placements of RBE2 and RBE3; **e** detail showing arm dimensions

the airframe. The most relevant articles in the latter category are summarised in Table 6 in the Appendix.

Most of these articles considered pre-established architectures, with the most common being a quadcopter. For dimensioning, some authors only considered hovering, take-off, or landing, whereas others included impacts and turns. As seen in the Appendix, there was no evidence of the implementation of IR, which was surprising considering that during its operation, the structure is in the air, meaning that BCs are not involved. Most authors studied or optimised the structure through BC-design: some fixed either the centre or the arm, whereas others split the model into components and analysed them independently.

Researchers who carried out optimisations typically started with pre-established architectures. In other words, the DS is very narrow, limiting the opportunity to obtain structures with higher performance. Based on this literature review, the study of Regino Prado was chosen [23] since it provided the most detailed information needed to reconstruct the model.

6.1 Information on the model

The drone had an X-type octocopter architecture, as shown in Fig. 10a. Initially, the DS for the optimisation focused on the arms (Fig. 10b, d and e); this was then expanded to form a square, with a height of 40 mm, as illustrated in Fig. 10c.

For the methodology, the list of components and their respective masses is summarised in Table 3. The material used was PA6F, which has the following mechanical properties: Young's modulus of 7453 MPa, Poisson's coefficient of 0.43, density of $1.29e-3g/mm^3$, and yield strength of 105 MPa.

Table 4 summarises the 16 load cases applied through RBE2 as shown in Fig. 10d. In the first 4 cases, forces are positive and follow the direction of the Y-axis; the moments are assigned according to the rotation of each motor, as shown in Fig. 10a. The last 3 cases are applied to each RBE2 at the bottom of the arms, and the forces are oriented along their local coordinate system (x_i, z_i), as shown in Fig. 11b.

Table 3 List of components with their masses

No	Component	Dim (mm)	Qty	Mass (g)	Perc (%)
1	Frame ZD550	550 × 395	1	675	24
2	Motor 2312 1150 kV	23 × 12	8	480	17
3	Propeller 9050	229	8	56	2
4	LiPo battery	1637 × 43 × 34	1	436	16
5	Speed controller (ESC)	68 × 24	8	132	5
6	Flight controller	82 × 47 × 16	1	41	1
7	Others			980	35
Total	2800	100			

Table 4 Flight load cases for optimisation

Drone loading conditions									
Load case		Force (N)				Moment (Nmm)			
		1–6	2–5	3–8	4–7	1–6	2–5	3–8	4–7
1	Max. performance	10.3				160			
2	Roll right	9.8	10.3	9.8		153	160	153	
3	Pitch forward	10.3		9.8		160	153	153	
4	Yaw	10.3	9.8	10.3	9.8	160	153	160	153
5–8	Impact X	200							
9–12	Impact Y	200							
13–16	Impact Z	200							

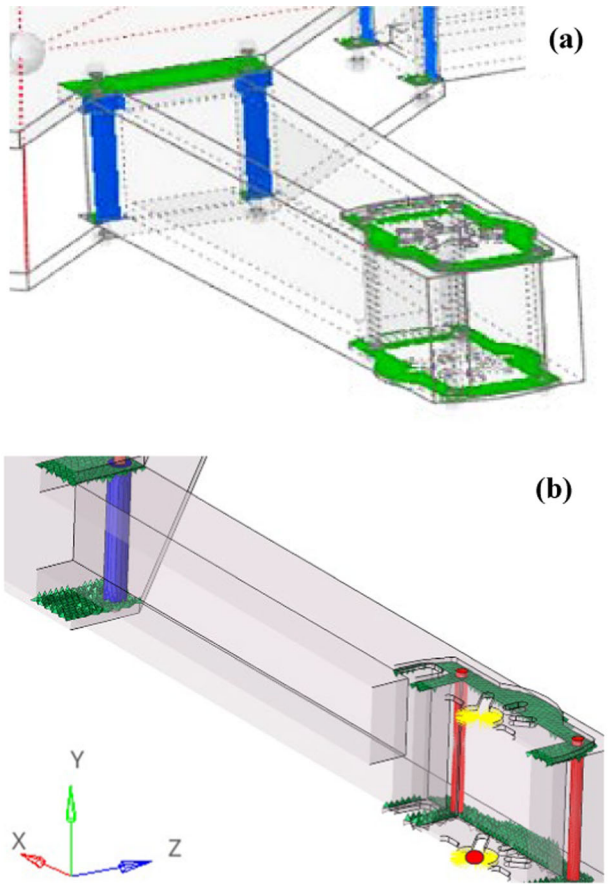

Fig. 11 **a** Original DS [23]; **b** reconstructed model (green and blue represent the sliding and the tied contact, respectively; yellow and red show RBE2 for the load and bolt connections, respectively; the red point shows the application of impact loads

6.2 First scenario: same DS

6.2.1 Model structure

In this case, the DS, contact, bolts, symmetries, and BCs are the same as shown in Fig. 11. Besides, to connect the body plates to the arms, RBE3 elements were selected, since when RBE2 was used, the central plates of the body had no stresses. The FEM model contained CHEXA8 elements, where the size of the arm was 1.5 mm, and the body plates were 4.5 mm.

In the original thesis, the author conducted a 2-step optimisation process [23]: in the first step, formulation ($\mathbb{P}_1$) was applied, within a volume constraint of 30%; the second step introduced another formulation ($\mathbb{P}_3$) based on the P-norm of the von Mises stresses σ^{PN} [39]. The objective was to minimise the mass while ensuring that the global stress was below $\overline{\sigma} = 66\mathrm{MPa}$, as illustrated in Eq. 15. The previously obtained structure was employed as the new DS for this step. The MinDim parameter was set to 4.5, while the MaxDim parameter was set to 30.

$$\begin{cases} \min m(\eta) = \sum_{i=1}^{N} v_i \eta_i \\ s.t. \begin{cases} [K]\{u\} = \{F_{ext}\} \\ \sigma^{PN}(\eta) \leq \overline{\sigma} \end{cases} \end{cases} \tag{15}$$

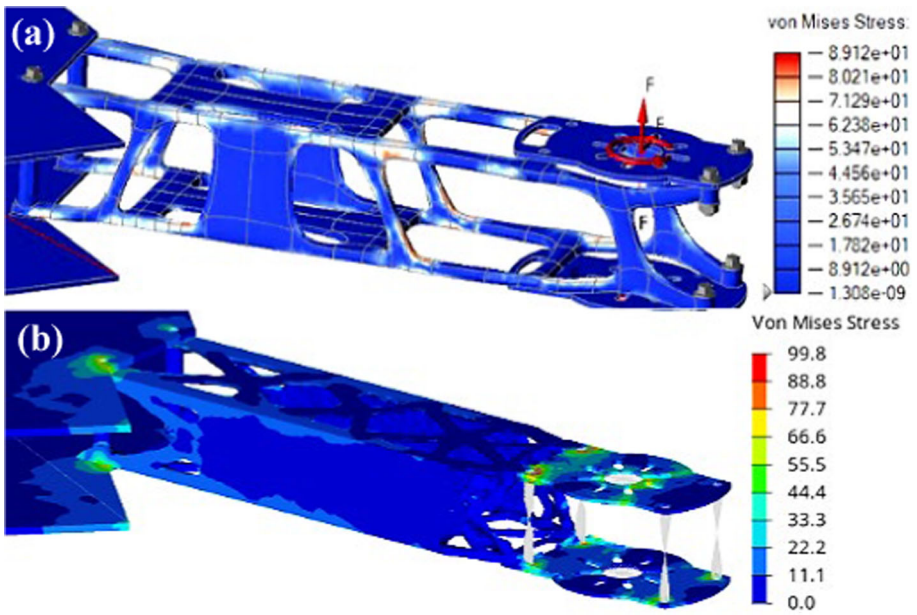

Fig. 12 Von Mises stresses (MPa); **a** original model [23]; **b** reconstructed model

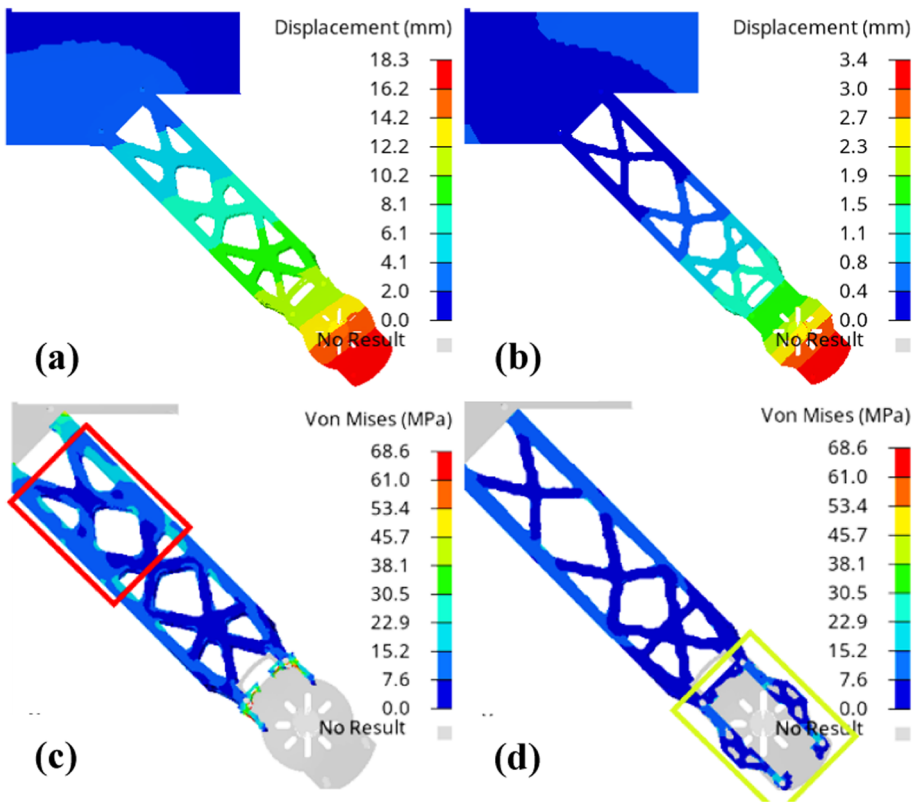

Fig. 13 Comparison of displacements for the **a** BC and **b** IR designs and equalised von Mises stress for the **c** BC-design and **d** IR-design

6.2.2 First optimisation results

When these 2 optimisation steps were complete, a comparison with the original work revealed significant disparities. When the threshold was applied to achieve the desired mass of 160 g, the reconstructed topology had a missing area, as shown in Fig. 12b. The stresses in the body and motor supports were also inconsistent with the original author's findings for the higher load case (labelled 'Impact Y'). This discrepancy can be attributed to the use of different software, in which diverse fastener setup options were available. As there was insufficient information about their mechanical behaviour, it was not possible to replicate the original model exactly. The model recreated in HyperWorks was used for

the subsequent studies, and the following analyses and comparisons refer to this model.

6.2.3 Inertia relief vs. traditional optimisation

After optimisation, both models achieved the desired mass of 160 g. However, as expected, the IR-design underwent 81.4% less strain than the BC-design, as shown in Fig. 13a and b. Moreover, by eliminating the stress concentrations observed in the BC-design, it was revealed that the stresses (100 MPa) in the structure were 31.4% higher than those in the IR-design. Figure 13c and d show that when the displayed stress values were equalised between the 2 models, the field distribution was more uniform in the IR-design.

6.3 Second scenario: methodology application

In this section, the first 4 steps of the methodology are applied to a 2D model. The remaining ones are then applied to a 3D model.

- Steps 1 and 2 of the methodology (namely specifications and load cases) were done by the author of the original paper.
- In Step 3, the architectural optimisation, the components remained in their original positions. Their central connection with the structure was modified as shown in.
- In Step 4, the DS was enlarged to take the shape of a square and increased by 75 mm following the arm direction, as shown in Fig. 10b.

6.3.1 2D model: pre-study for efficient model setup

Considering the parameters involved in TO, Sect. 2.2, this step assists in setting up the models and selecting the most relevant parameters. The use of 2D models allows for a reduction in the dimensionality. Consequently, the number of nodes and the computation time required. In this approach, the DS becomes a shell with a 40 mm thickness.

6.3.1.1 BC-design The RBE2 elements were replaced with RBE3, as shown in Fig. 14. The loads and moments are applied to the dependent node, positioned at the CG of the motors, 34 mm from the plane in the Y-direction. Independent nodes are placed at the attachment points of the motor, as shown in Fig. 10d.

To explore Steps 4 and 5 of the methodology, 3 different model setups were created. Models 11 × featured a square DS with a central RBE3 motor-oriented configuration, while in models 12 × , this was rotated by 45°. In models 13x, the DS had a circular shape with a diameter that equals the previous models' diagonal. The (x) in the models represents

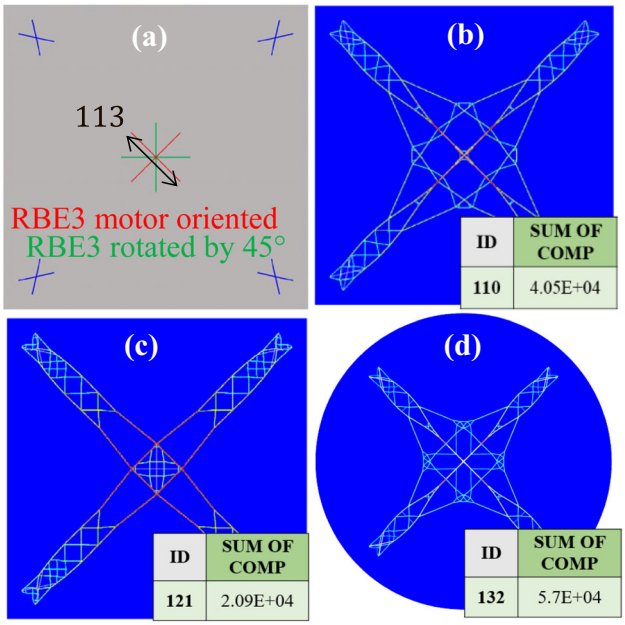

Fig. 14 BC-design topology results: **a** RBE3 applications; **b** model 110; **c** model 121; **d** model 132

the 10 configurations to evaluate the parameters Mindim, MaxDim and MinGap. TO was performed in one step with the formulation ($\mathbb{P}_1$), where the constraint was a maximum mass of 300 g.

For reconstruction, a threshold ranging between 0.2 and 0.25 was applied. The mass of the structure reached 400 g. A comparison of the results shows that model 110 exhibited the lowest stresses, as depicted in Fig. 15a. Furthermore, it is evident that increasing the size of the DS reduced the displacement by 65%, from 18.3 mm to 6.39 mm, and the stress magnitude by 58%, from 100 MPa to 41.9 MPa.

6.3.1.2 IR simulation: initial modelling In this step, different TO formulations were evaluated: (i) ($\mathbb{P}_1$); (ii) ($\mathbb{P}_3$); (iii) compliance minimisation under a displacement constraint; and (iv) compliance minimisation under a displacement plus a stress constraint. The resulting topologies depict structures that do not cross the CG and are directed towards the DS edge, as shown in Fig. 16. This concentration can be attributed to the absence of loads or masses representing the components at the CG; alternatively, it could be inferred that this configuration is well-suited to the defined load cases because it increases the structure inertia. Based on this observation, we propose that for a new drone concept, components should be designed, adapted, and positioned following this novel architecture to take full advantage of its inherent structural rigidity.

6.3.1.3 Enhanced IR modelling: adding the masses of the main components In Steps 3 and 5 of the methodol-

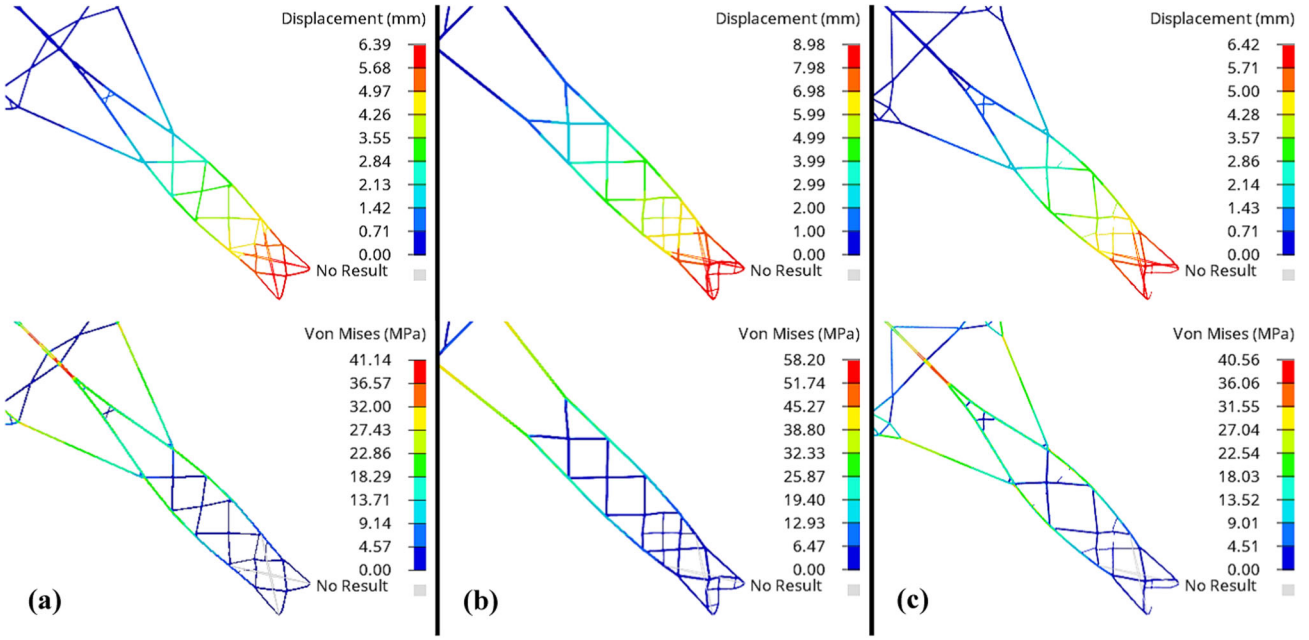

Fig. 15 Displacements and stresses for the reconstructed topologies of the BC-design: **a** model 110; **b** model 121; **c** model 132

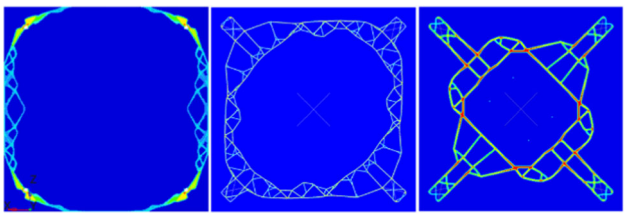

Fig. 16 TO results for the IR-design without the masses of the components

ogy, it is important to consider the positions of the electronic components, as presented in Table 1. The main masses were assigned according to the original author's work: motors and propellers with a mass of 67 g were placed at nodes 1–8, while the remaining components were concentrated at the centre of the DS with a mass of 1589 g, as shown in Fig. 10. Formulation ($\mathbb{P}_1$) remained, and 3 variations (31x, 32x, and 33x) were created to compare with the BC configurations.

From Fig. 17, the inclusion of masses in the model results in a well-defined structure, with a noticeable stress field extending from the motors to the CG. The orientation of the central RBE3 also has a significant impact on the compliance of the structure.

6.3.1.4 Comparison between BC-design and IR-design To summarize, for the same parameters and DS, the optimised IR models have lower compliance. On average, the compliance for the IR models is approximately $1.79E04$, while for BC models, it is $3.95E04$, resulting in a reduction of 54.7%. As observed above, the models with a central RBE3

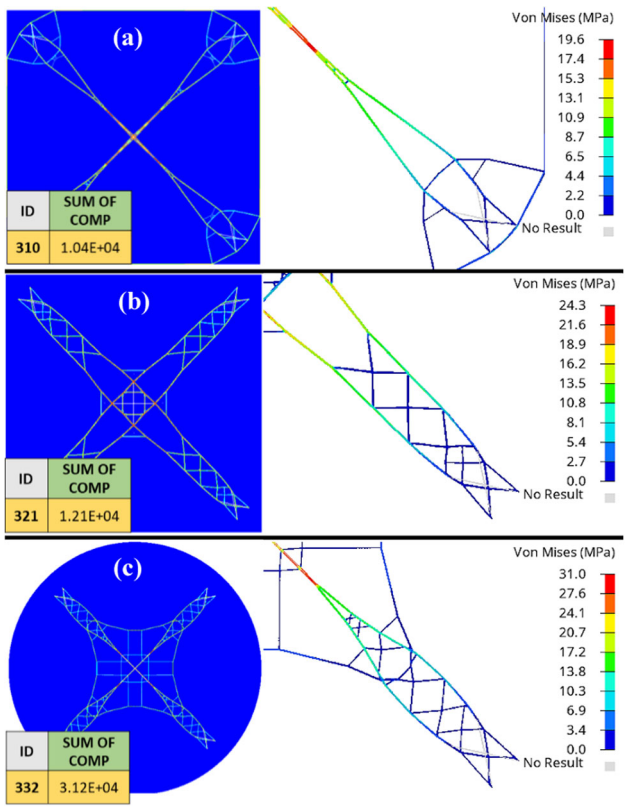

Fig. 17 TO and static results for IR-design models: **a** model 310; **b** model 321; **c** model 332

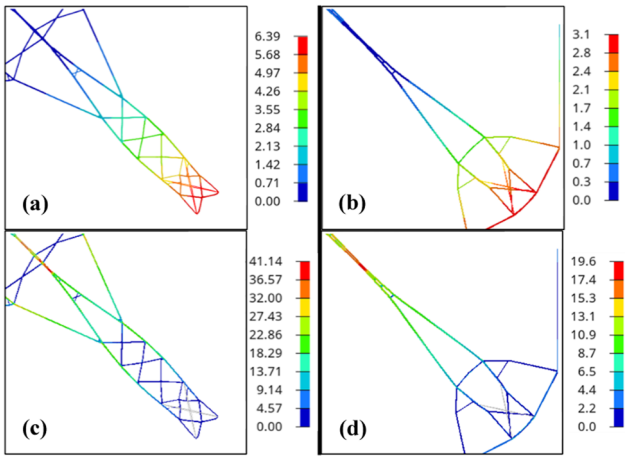

Fig. 18 Static analysis of reconstructed structures, with displacements in mm **a**, **c** model 110; and stresses in MPa **b**, **d** model 310

motor-oriented were the stiffest. These structures were therefore selected for comparison, with models 11X representing the BC-design and models 31X representing IR-design. Figure 18a shows that the displacement was 51.3% higher in the BC-design than in the IR-design (6.39 mm compared to 3.11 mm, (Fig. 18b). Similarly, the stresses obtained from the BC model are 53% higher (41.1 MPa) compared to the IR model (19.6 MPa), as shown in Fig. 18d.

6.3.1.5 Preliminary conclusions The proposed pre-study approach serves as a valuable guide for new designers, as it facilitates the exploration of concepts, modelling techniques, and formulation. Besides, it was determined that the optimal configuration required the central RBE3 to be oriented towards the motors; however, the 2D model does not allow the components to be placed centrally. Thus, the next step involved transitioning to a 3D model.

6.3.2 3D model: final steps in the methodology

In this section, the last steps of the proposed methodology are applied as follows:

- *Step 4* As mentioned above, a hole was created in the DS to accommodate the large component located in the middle. The hole leaves a 5 mm distance for the fixing of the central components, as shown in Fig. 19b. In this model, there is no NDS.
- *Step 5* involves the positioning of the masses of the electronic components and the transmission of loads.

It can be observed that the components are not located in the same plane. It is therefore necessary to include the mass of each electronic component positioned at its CG, as

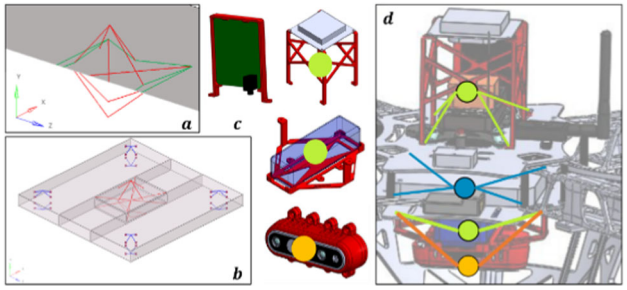

Fig. 19 Modelling of new electronic components: **a** 2D model; **b** 3D model; **c** representation of masses; **d** positioning of RBE3s

shown in Fig. 19d. At the bottom, there is the camera, followed by the battery. In the middle, there is the ESC and the flight controller, with two-thirds of the other components. The remaining one-third is located at the top. New RBE3 elements are created to connect each concentrated mass to the structure.

- *Steps 6 and 7* The model contains CHEXA8 elements sized at 1.5 mm. Formulation $\mathbb{P}_1$ is applied, with a constraint of 300 g. The MinDim parameter was set to 4.5, and MaxDim to 10.
- *Step 8* This is the performance validation step.

Reconstruction was performed with a threshold of 0.25, achieving a mass of 350 g. In terms of topology, Fig. 20 demonstrates that the BC-design does not preserve material for future structural attachments in the same way as IR-design. This can be considered as a disadvantage, since additional redesign or modification of the initially planned positions may be required, such as new attachments points on the structure, as shown in Fig. 20a, in contrast to Fig. 20b.

When the 2 obtained structures are superimposed, as shown in Fig. 21, several differences become apparent, which can be attributed to the different methods of load calculation. In IR, the elastic forces are calculated by considering the inertia and masses. This explains why the IR-design model retains more material in the motor zone to counteract the applied loads, as can be seen from Fig. 21c, while the BC-design model incorporates stiffeners that extend from the centre towards the arms (Fig. 21b). Moreover, at the bottom of the IR structure, a bar connects all the arms of the drone, as can be seen in Fig. 21b. This design optimisation may be intended to counteract the displacements caused by the perpendicular impact load.

From a comparison of the results of a static analysis, it is evident that the 3D model has global lower values than the 2D model. This can be attributed to the advantages of the 3D model in terms of element distribution and density .

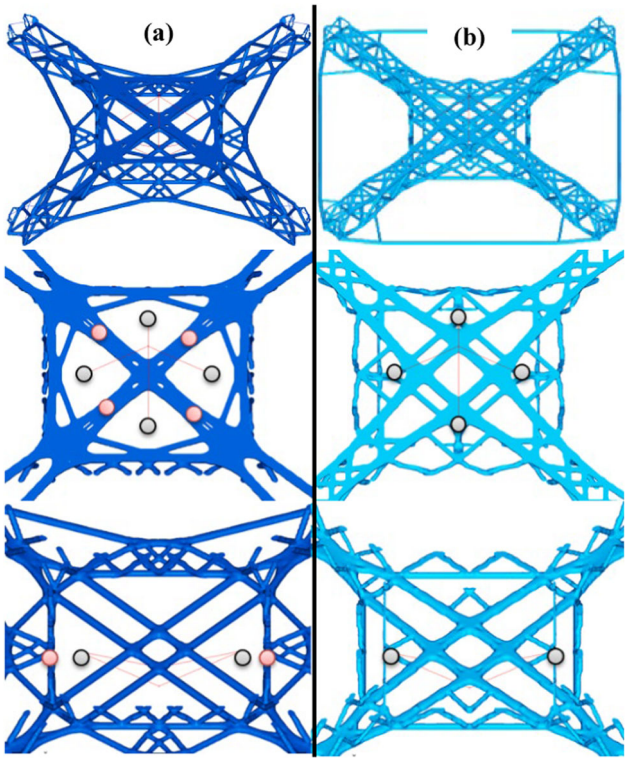

Fig. 20 Attachment points for electronic components: **a** BC-design (dark blue); **b** IR-design (light blue)

- *Steps 9 and 10* are outside the scope of this study.

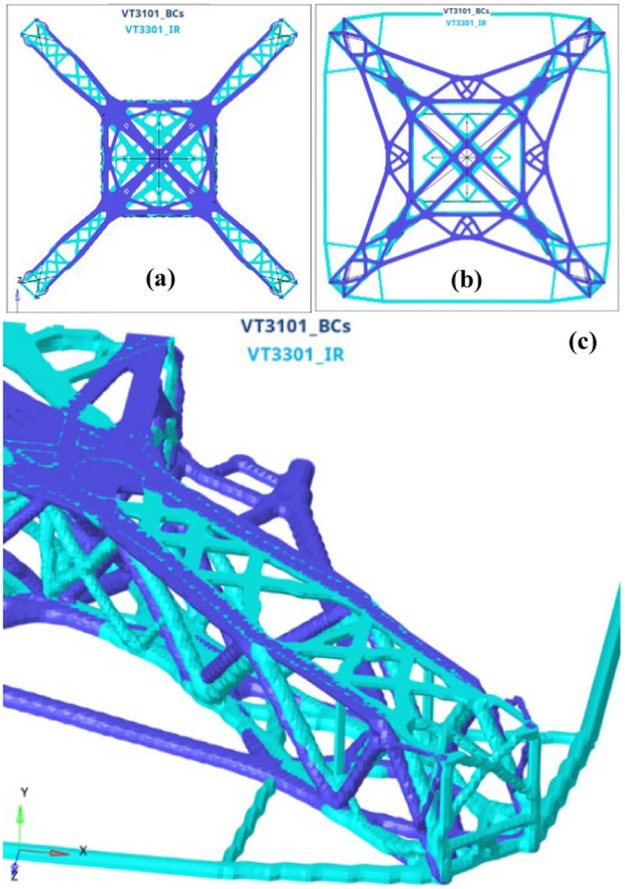

Fig. 21 Comparison of topologies created with the BC-design (dark blue) and IR-design (light blue); **a** top view; **b** bottom view; **c** arm detail

7 Discussion

Using the first 2 examples, we demonstrated how BC-design can degrade the mechanical behaviour of an US. For the suspension arm, the reduction in the inertial properties of up to 37% could contribute to an increase of 53% in the deformation energy of the model obtained by BC-design. This effect was also observed in the second example, where the compliance obtained under IR-design was 37% lower than for the BC-design, and the first eigenfrequency was 8.5% higher.

For the drone, Table 5 shows the results and gains for each study and model. The enlargement of the DS together with IR-design optimisation gives a reduction of 79% of the maximum stress compared to the original work of Regino, as indicated by [5]. Moreover, the 2D and 3D models give comparable gains in terms of average stresses, with 52% for the former and 72% for the latter in comparison to the BC-design models. The 3D model also achieved a reduction in the airframe mass by 12.5%. This guarantees a better service life, thanks to a higher safety coefficient demonstrating the interest of considering the impact of IR + TO on unconstrained structures.

Regarding the displacements, we note that the IR-design again outperformed the BC-design. The overall values for the IR model were 24% lower, and in the critical zone of the motor mount the difference was 42%, as shown in Fig. 22. For the stresses, we observe that for the most critical load case (Impact Y), the values are 72% higher in the BC-design (Fig. 23a). This may be related to the stress concentration. To facilitate a comparison between them, reference points were selected and depicted in Fig. 23. For instance, in the motor joint area, the stress difference ranges from 27 to 60%. Similarly, when comparing stress values in the arm areas, the difference is approximately 45%. When the stress values of the BC-design are adjusted to match those obtained in the IR-design (12.8 MPa), it becomes evident that there are more zones with higher stresses and a less uniform distribution in the former.

The differences in the previous results, and the enhanced performance of the IR-designs, can be attributed to (i) the application of load cases at a considerable distance from the CG results in higher acceleration values in the motor zone

Table 5 Summary of results

Tech. analysis	Displacement (mm)			Stress (MPa)			Mass (g)
	BC	IR	Δ%	BC	IR	%	
Orig. opt	18.3	3.4	81.4	100.0	68.6	31.4	400
2D DS	6.4	3.1	51.6	41.1	19.6	52.3	400
3D DS	3.3	1.9	42.4	46.0	12.8	72.2	350

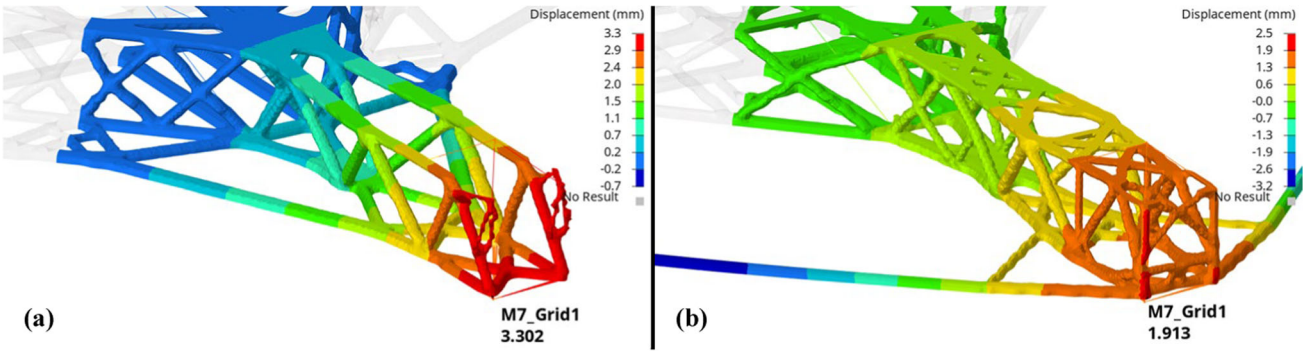

Fig. 22 Y-displacements of reconstructed structures: **a** BC-design; **b** IR-design

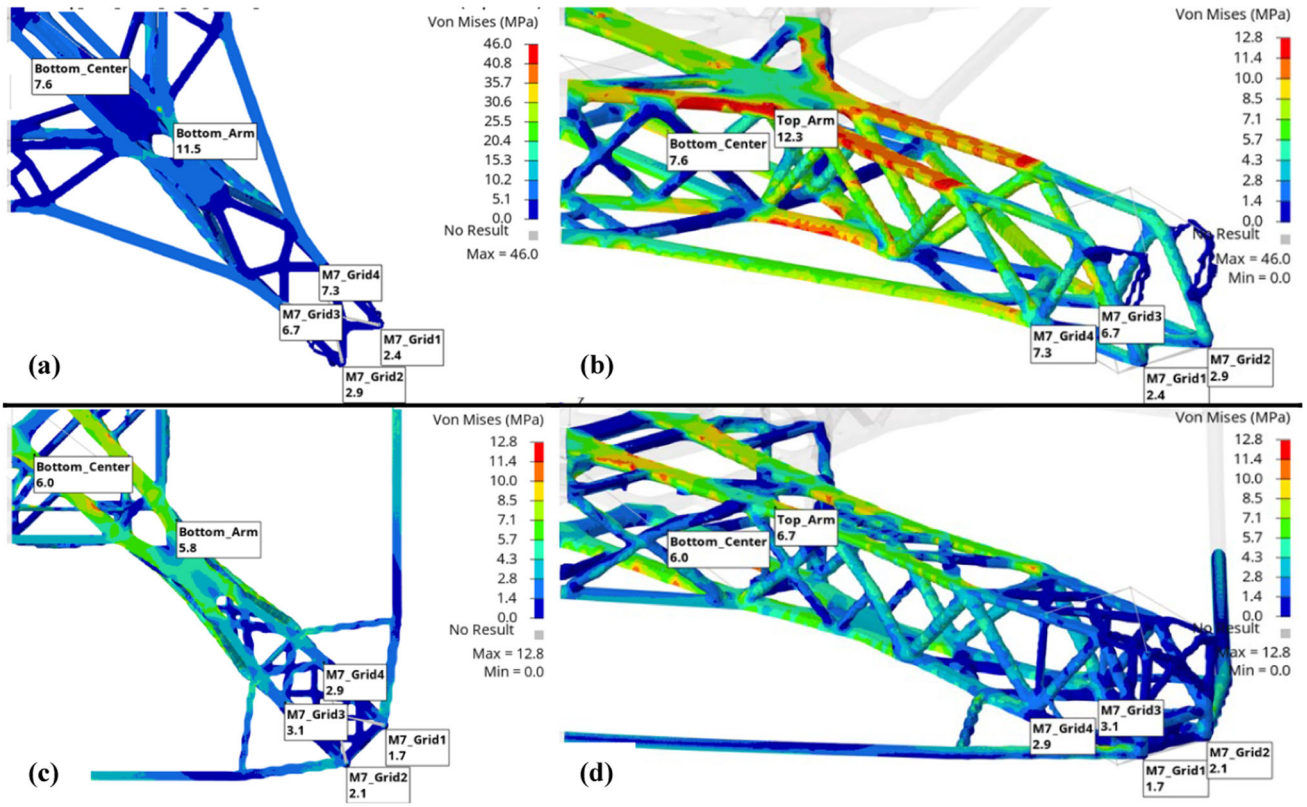

Fig. 23 Von Mises stress fields for reconstructed structures: BC-design: **a** top; **b** ISO; IR-design: **c** top; **d** ISO

according to the RB transformation matrix $\left[\Phi_{i,0}\right]$, as previously discussed in Sect. 2.1; (ii) this phenomenon leads to a greater concentration of material to counteract the applied loads, as evidenced by [26] in Sect. 2.3. Consequently, the entire body, including the interconnected arms, participates in the load-bearing structure; in contrast, the BC-design relies on stiffeners to reinforce the arms, as previously mentioned. These results are also supported by [19], which states that in instances where the relative significance of inertial loads in comparison to other loads is considerable, optimal designs for USs diverge significantly from those optimised for static conditions.

8 Conclusions

This study has demonstrated the advantages and importance of the optimisation of USs employing IR. The mathematical development emphasised the influence of the applied loads and masses on the stress calculations. Two examples were considered to explore the impact of applying BCs and the benefits and considerations associated with structure optimisation using IR. The first example showed that to maintain a connecting region, it is necessary to apply the loads or the mass of the component to be connected or set a NDS. The second example highlighted the significant improvements in inertia obtained through the use of IR, as well as reductions in the stresses. This led to the proposal of an optimisation methodology, which was applied to the case study of a quadcopter structure.

In addition, conducting a preliminary study with a simplified (2D) model aids in identifying the best modelling setup and parameters, which saves time in terms of iterations compared to a direct implementation with a 3D model. Moreover, increasing the DS allows for new topologies that make better use of available material, leading to a further reduction in the total mass of the drone.

The results of the case study indicated a total weight reduction of approximately 325 g compared to the original model and 50 g compared to a classically optimised one, corresponding to weight reductions of 48.5% and 12.5%, respectively. In the most critical load case (impact in the Y direction), the maximum displacements of the arm, where the motor support is located, were reduced by 42%, and the stresses were reduced by 45% on average, with a maximum reduction of 60%. Although we do not consider manufacturing or assembly concerns here, we can infer that the mass reduction will offset any increase in the joint areas.

Finally, a comparison of the 2 topologies obtained using the BC and IR approach proved that the latter adapts much better to extreme conditions, such as impact cases.

9 Outlook

Limitations on the scope of this article prevent from studying the positions of the electronic components. They could be strategically placed to balance the structure based on their mass and inertia. This placement would allow to obtain a structure adapted to the stresses induced by each component, considering at the same time their respective connection areas.

Since the last 2 steps of the methodology were not implemented, it would be important to explore different methods of splitting the structure. One possible approach could involve starting with larger frames or those having lower stresses and strains. Additionally, exploring considerations for AM to better support new designers in the redesign of unconstrained structures.

Appendix

See Table 6.

Table 6 Literature review of design and optimisation of drone airframes

Source	References	IR	BCs	Struct. shape	Dimensions	Comp. mass	Material property	Opt	Model config	Load cases	Load appl	Load values
Art	[40]		A-Bdc	Quad–X			E, ν, ρ, σ_y		Assembly	Take-off	Arm-body Connection (A-Bdc)	Yes
	[41]		Legs	Hex			PE	TO	One-Body	Take-off	Motors	Yes
	[42]		A-Bdc	Modular		Yes	E, ν, ρ, σ_y		Arm	Take-off	Motors	Yes
	[20]		Body	Quad–X	Body, arms	Yes		TO	One-Body	Hovering	Motors	Yes
	[43]	Yes		Octo–X	Body	Yes		TO	One-Body	Hovering	Motors	Yes
	[44]		A-Bdc	Quad–H			E, ν, ρ, σ_y	GD	Assembly	Landing Lifting	Motors	Yes
	[45]		Body	Quad–X	Body, arms		ABS		Assembly	Take-off, Impact	Motors	Yes
	[46]		Motors	Quad–X	Body	Yes			Assembly	Take-off	Body	
	[47]			Quad–X	Body, arms		Al-7075		Assembly			
	[48]		Legs	New Arch			E, ν, ρ, σ_y		Assembly	Take-off	Motors	Yes
	[49]		- A-Bdc *Body	Quad–X	Body		Al alloys		- Arms *Assembly	Take-off	Motors	Yes
	[50]		Body	Quad – H			E, ν, ρ, σ_y	TO	Body	Take-off	Motors	Yes
	[51]			Tricopter			E, ν, ρ, σ_y		Assembly	Impact		Yes
Conf	[52]		- Body *Arms	Quad–X	DJI-F450	Yes	E, ν, ρ		Assembly	Take-off	Body	
	[53]		- Body *Arms	Quad–X			E, ν, σ_y		One-Body	1) Take-off 2) Hovering	1) Arms, 2) Body	Yes
	[22]		Body	Quad–X	DJI-F450	Yes	ABS	GD	One-Body	Take-off	Arms	Yes
	[54]		Body	Quad–X	Body		E, ν, σ_y		One-Body	Impact	Motors	
	[55]		Body	Quad–X	Body		E, ν, σ_y	TO	One-Body	Take-off	Motors	Yes
	[21]		A-Bdc	Quad–X			Al-7075	TO	One-Body	1) Take-off, Hovering Turns, Forward flight 2) Full speed	1) Body 2) Motors	Yes

Table 6 (continued)

Source	References	IR	BCs	Struct. shape	Dimensions	Comp. mass	Material property	Opt	Model config	Load cases	Load appl	Load values
	[56]		Body	Quad–X			ABS		Arm	Hovering, Landing	Motors	
Univ	[57]		Arms Base	Quad–X	Body, arms, legs		E		Arm	Take-off	Motors	
	[58]		Motors	Quad–X	Body, arms		E, ν, ρ, σ_y	GD	One-Body	Hovering	1) Motors, 2) Body	
	[23]		Body	Octo–X, H, I	Body, arms, legs	Yes	E, ν, ρ, σ_y	TO	Assembly	Take-off, Hovering Impact, Turns	Motors	Yes

Acknowledgements This work was supported by funding from the University of Toulon, COSMER laboratory—RNSR201522018X, and Expleo Group.

Funding Open access funding provided by Université de Toulon.

Data availability The results presented can be replicated using the software HyperWorks 2022 by Altair. The data will be available once requested.

Declarations

Conflict of interest No potential conflict of interest was reported by the author(s).

References

1. Renjith, S.C., Park, K., Okudan Kremer, G.E.: A design framework for additive manufacturing: integration of additive manufacturing capabilities in the early design process. Int. J. Precis. Eng. Manuf. **21**(2), 329–345 (2020). https://doi.org/10.1007/s12541-019-00253-3
2. Bendsøe, M.P., Kikuchi, N.: Generating optimal topologies in structural design using a homogenization method. Comput. Methods Appl. Mech. Eng. **71**(2), 197–224 (1988)
3. Deaton, J.D., Grandhi, R.V.: A survey of structural and multidisciplinary continuum topology optimization: post 2000. Struct. Multidiscip. Optim. **49**(1), 1–38 (2014). https://doi.org/10.1007/s00158-013-0956-z
4. Morretton, E., Vignat, F., Pourroy, F., Marin, P.: Impacts of the settings in a design for additive manufacturing process based on topological optimization. Int. J. Interact. Des. Manuf. **13**(1), 295–308 (2019). https://doi.org/10.1007/s12008-018-00524-9
5. Tyflopoulos, E., Steinert, M.: Messing with boundaries - quantifying the potential loss by pre-set parameters in topology optimization. Procedia CIRP **84**, 979–985 (2019). https://doi.org/10.1016/j.procir.2019.04.307
6. Orquéra, M., Albrand, F., Lasso, C., Millet, D., Campocasso, S.: Advanced optimisation of a mechanical product for its additive manufacturing. Int. J. Interact. Des. Manuf. (2023). https://doi.org/10.1007/s12008-023-01232-9
7. Prathyusha, A.L.R., RaghuBabu, G.: A review on additive manufacturing and topology optimization process for weight reduction studies in various industrial applications. Mater. Today Proc. **62**, 109–117 (2022). https://doi.org/10.1016/j.matpr.2022.02.604
8. Zhu, J., Zhang, W., Xia, L.: Topology Optimization in aircraft and aerospace structures design. Arch. Comput. Methods Eng. **62**, 595–622 (2016). https://doi.org/10.1007/s11831-015-9151-2
9. Matsimbi, M., Nziu, P.K., Masu, L.M., Maringa, M., Engineering, M.: Topology optimization of automotive body structures: a review. Int. J. Eng. Res. Technol. **13**(12), 4282–4296 (2020)
10. Barnett, A. R., Widrick, T. W., Damian, R.:Closed-form static analysis with inertia relief and displacement-dependent loads using a MSC/NASTRAN DMAP alter. 1995
11. Lee, Y. L., Guo, M.: Pseudo stress analysis techniques. Elsevier Inc., 2012
12. Wijker, J.:Free-free dynamic systems, inertia relief. Mech. Vib. Spacecr. Des. 2004, pp. 303–311
13. Nelson, M.F., Wolf, J.A.: The use of inertia relief to estimate impact loads. SAE Tech. Pap. (1977). https://doi.org/10.4271/770604
14. De, S., et al.: Lightweight chassis design of hybrid trucks considering multiple road conditions and constraints. World Electr. Veh. J. **12**(1), 1–20 (2021). https://doi.org/10.3390/WEVJ12010003
15. Liao, L.:A study of inertia relief analysis. In: 52nd AIAA/ASME/ASCE/AHS/ASC structures, structural dynamics and materials conference 19th AIAA/ASME/AHS adaptive structures conference. no. April, pp. 1–10, 2011, https://doi.org/10.2514/6.2011-2002
16. Pagaldipti, N., Shyy, Y. K.:Influence of inertia relief on optimal designs. no. September, pp. 1–6, 2004

17. Wagner, N., Helfrich, R. Topology optimization based on inertia relief analysis. 2017
18. Song, W., Gea, H. C., Yang, R., Chuang, C.:Application of regional strain energy in topology optimization with inertia relief analysis. In: Proceedings of the ASME design engineering technical conference, 2013, pp. 1–9
19. Thore, C.J.: Topology optimization of freely floating elastic continua using the inertia relief method. Comput. Methods Appl. Mech. Eng. **361**, 112733 (2020). https://doi.org/10.1016/j.cma.2019.112733
20. Esakki, B., Mathiyazhagan, S., Moses, M., Jagajjanani Rao, K., Ganesan, S.: Development of 3D-printed floating Quadrotor for collection of algae in remote water bodies. Comput. Electron. Agric. **164**, 104891 (2019). https://doi.org/10.1016/j.compag.2019.104891
21. Qu, J., Dong, Y., Gu, X., He, S.: Integrated frame topology optimization design of small quadrotor UAV. J. Phys. Conf. Ser. **2292**(1), 012016 (2022). https://doi.org/10.1088/1742-6596/2292/1/012016
22. Bright, J., Suryaprakash, R., Akash, S., Giridharan, A.: Optimization of quadcopter frame using generative design and comparison with DJI F450 drone frame. IOP Conf. Ser. Mater. Sci.Eng. **1012**(1), 012019 (2021). https://doi.org/10.1088/1757-899x/1012/1/012019
23. Regino Prado, J. L.: Economic optimization of drone structure for industrial indoor use by additive manufacturing. Master's thesis, Politecnico di Torino, 2022.
24. Han, H., Guo, Y., Chen, S., Liu, Z.: Topological constraints in 2D structural topology optimization. Struct. Multidiscip. Optim. **63**(1), 39–58 (2021). https://doi.org/10.1007/s00158-020-02771-5
25. Vatanabe, S.L., Lippi, T.N., Lima, C.R.D., Paulino, G.H., Silva, E.C.N.: Topology optimization with manufacturing constraints: a unified projection-based approach. Adv. Eng. Softw. **100**, 97–112 (2016). https://doi.org/10.1016/j.advengsoft.2016.07.002
26. Quinn, G. C.:Full automobile topology design optimized to maximize structural stiffness subject to multiple static load cases including inertial relief. In: 13th AIAA/ISSMO multidisciplinary analysis and optimization conference, 2010, no. September, pp. 9361–9377, https://doi.org/10.2514/6.2010-9361.
27. Altair, RBE2s, RBE3s, and MPCs, 2021. https://2021.help.altair.com/2021/hwdesktop/hwx/topics/pre_processing/model_build_and_assembly/rbe2_rbe3_mpc_c.htm (accessed Oct. 23, 2023).
28. Altair,OS-T: 1030 3D Inertia relief analysis. 2022. https://2022.help.altair.com/2022/hwsolvers/os/topics/solvers/os/3d_inertia_relief_analysis_r.htm#Z_3d_inertia_relief_analysis_r (accessed May 02, 2023).
29. Altair, Design optimization Responses. 2021. https://2021.help.altair.com/2021/hwsolvers/os/topics/solvers/os/responses.htm (accessed Oct. 26, 2023).
30. Lasso Perdomo, C. J., Millet, D., Orquera, M., Gabriel, B., De Dominici, G.: Could the airframe of the future be made of metal only? potential of AM in the helicopter domain. In: Advances on mechanics, design engineering and manufacturing IV. JCM 2022. lecture notes in mechanical engineering, 2023, pp. 967–979, https://doi.org/10.1007/978-3-031-15928-2_85.
31. Orquéra, M., Campocasso, S., Millet, D.: Design for additive manufacturing method for a mechanical system downsizing. Procedia CIRP **60**, 223–228 (2017). https://doi.org/10.1016/j.procir.2017.02.011
32. Kumke, M., Watschke, H., Vietor, T.: A new methodological framework for design for additive manufacturing. Virtual Phys. Prototyp. **11**(1), 3–19 (2016). https://doi.org/10.1080/17452759.2016.1139377
33. Federal Aviation Administration, Weight and Balance Handbook, Faa-H-8083–1B. U.S. Department of Transporation, pp. 1–114, 2016
34. Ramsaier, M., Stetter, R., Till, M., Rudolph, S.: Automatic definition of density-driven topology optimization with graph-based design languages. In: Advances in structural and multidisciplinary optimization. WCSMO 2017, 2018, vol. 1, pp. 1168–1184
35. Whiteside, S. K. S. *et al.*, Design of a tiltwing concept vehicle for urban air mobility. 2021.
36. Reichwein, J., Rudolph, K., Geis, J., Kirchner, E.: Adapting product architecture to additive manufacturing through consolidation and separation. Procedia CIRP **100**, 79–84 (2021). https://doi.org/10.1016/j.procir.2021.05.013
37. Hassanalian, M., Abdelkefi, A.: Classifications, applications, and design challenges of drones: a review. Prog. Aerosp. Sci. **91**, 99–131 (2017). https://doi.org/10.1016/j.paerosci.2017.04.003
38. Goh, G.D., Agarwala, S., Goh, G.L., Dikshit, V., Sing, S.L., Yeong, W.Y.: Additive manufacturing in unmanned aerial vehicles (UAVs): challenges and potential. Aerosp. Sci. Technol. **63**, 140–151 (2017). https://doi.org/10.1016/j.ast.2016.12.019
39. Holmberg, E., Torstenfelt, B., Klarbring, A.: Stress constrained topology optimization. Struct. Multidiscip. Optim. **48**(1), 33–47 (2013). https://doi.org/10.1007/s00158-012-0880-7
40. Anudeep, M., Diwakar, G., Katukam, R.: Design of a quad copter and fabrication. Int. J. Innov. Eng. Technol. **4**(1), 59–65 (2014)
41. Bajirao, M.S., Vijay, K.P., Sudhir, G.R.: Design optimization of drone frame. Int. J. Mech. Des. **8**(1), 25–32 (2022)
42. Brischetto, S., Torre, R.: Preliminary finite element analysis and flight simulations of a modular drone built through fused filament fabrication. J. Compos. Sci. **5**(11), 293 (2021). https://doi.org/10.3390/jcs5110293
43. Guo, H., Li, M., Sun, P., Zhao, C., Zuo, W., Li, X.: Lightweight and maintainable rotary-wing UAV frame from configurable design to detailed design. Adv. Mech. Eng. **13**(7), 1–10 (2021). https://doi.org/10.1177/16878140211034999
44. Mohamedzain, A.O., Chua, H., Yap, K., Uthayasurian, P., Jiehan, T.: Novel drone design using an optimization software with 3D model, simulation, and fabrication in drone systems research. Drones **6**(4), 97 (2022). https://doi.org/10.3390/drones6040097
45. Parandha, S.M., Li, Z.: Design and analysis of 3D printed quadrotor frame. Int. Adv. Res. J. Sci. Eng. Technol. **5**(4), 66–73 (2018). https://doi.org/10.17148/IARJSET.2018.5411
46. Shah, K.N., Dutt, B.J., Modh, H.: Quadrotor—an Unmanned Aerial Vehicle. Int. J. Eng. Dev. Res. **2**(1), 1299–1303 (2014)
47. Sharma, S., Srivastava, A.: Design and analysis of drone, Int. Res. J. Eng. Technol., pp. 3561–3566, 2021.
48. Sundararaj, S., Dharsan, K., Ganeshraman, J., Rajarajeswari, D.: Structural and modal analysis of hybrid low altitude self-sustainable surveillance drone technology frame. Mater. Today Proc. **37**, 409–418 (2020). https://doi.org/10.1016/j.matpr.2020.05.397
49. Vosniakos, G.C., Lekai, E., Maltezos, G.: On the mechanical design of a customized unmanned aerial vehicle transporter for flexible manufacturing systems. IFAC-Papers OnLine **55**(10), 989–994 (2022). https://doi.org/10.1016/j.ifacol.2022.09.485
50. Yap, Y.L., et al.: Topology optimization and 3D printing of micro-drone: numerical design with experimental testing. Int. J. Mech. Sci. **237**, 107771 (2023). https://doi.org/10.1016/j.ijmecsci.2022.107771
51. Zhang, Y., et al.: High-precision modeling and collision simulation of small rotor UAV. Aerosp. Sci. Technol. **118**, 106977 (2021). https://doi.org/10.1016/j.ast.2021.106977
52. Ahmed, M. F., Zafar, M. N., Mohanta, J. C.: Modeling and analysis of quadcopter F450 frame. In: 2020 international conference on contemporary computing and applications (IC3A), Feb. 2020, pp. 196–201, https://doi.org/10.1109/IC3A48958.2020.233296.
53. Alphonso, R. F., Irawan, A. P., Daywin, F. J.: Design and development of quadcopter prototype. In: 2nd international conference

on engineering of Tarumanagara (ICET 2015), 2015, no. 02, pp. 1162–1164.
54. Martinetti, A., Margaryan, M., van Dongen, L.: Simulating mechanical stress on a micro unmanned aerial vehicle (UAV) body frame for selecting maintenance actions. Procedia Manuf. **16**, 61–66 (2018). https://doi.org/10.1016/j.promfg.2018.10.160
55. Martinez Leon, A. S., Rukavitsyn, A. N., Jatsun, S. F.: UAV airframe topology optimization. In: 6th International conference on industrial engineering, 2021, no. ICIE 2020, pp. 338–346, https://doi.org/10.1007/978-3-030-54814-8_41.
56. Sharma, P., Arockia Selvakumar, A.: Conceptual design and nonlinear analysis of triphibian drone. Procedia Comput. Sci. **133**, 448–455 (2018). https://doi.org/10.1016/j.procs.2018.07.055
57. Kuantama, E., Craciun, D., Tarca, R.: Quadcopter body frame model and analysis. Ann. Univ. Oradea. Fascicle Manag. Technol. Eng. **15**(1), 71–74 (2016). https://doi.org/10.15660/auofmte.2016-1.3205
58. Obli, P. N.: Quadcopter frame optimization, Bachelor's Thesis, Dayananda Sagar College of Engineering, 2020